Synthesis of Non-centrosymmetric, Metastable Rare-Earth Oxysulfides by Anionic Redox Topochemistry

Louis-Béni Mvélé, Shunsuke Sasaki, Philippe Deniard, Yoshihiro Tsujimoto, Etienne Janod, Catherine Guillot-Deudon, Maria Teresa Caldes, Isabelle Braems, Benoit Corraze, Stéphane Jobic, et al.

To cite this version:

Louis-Béni Mvélé, Shunsuke Sasaki, Philippe Deniard, Yoshihiro Tsujimoto, Etienne Janod, et al.. Synthesis of Non-centrosymmetric, Metastable Rare-Earth Oxysulfides by Anionic Redox Topochemistry. Chemistry of Materials, 2023, 35 (18), pp.7597-7604. 10.1021/acs.chemmater.3c01299 . hal-04295062

HAL Id: hal-04295062

https://cnrs.hal.science/hal-04295062

Submitted on 22 Nov 2023

Synthesis of non-centrosymmetric, metastable rare-earth oxysulfides by anionic redox topochemistry

Louis-Béni Mvélé[1], Shunsuke Sasaki[1], Philippe Deniard[1], Yoshihiro Tsujimoto[2], Etienne Janod[1], Catherine Guillot-Deudon[1], Maria Teresa Caldes[1], Isabelle Braems[1], Benoit Corraze[1], Stéphane Jobic[1,*], Laurent Cario[1,*]

1. Nantes Université, CNRS, Institut des Matériaux de Nantes Jean Rouxel, IMN, F-44000 Nantes, France.

2. International Center for Materials Nanoarchitechtonics (WPI-MANA), National Institute for Materials Science (NIMS), Tsukuba, Ibaraki 305-0044, Japan

ABSTRACT: Intercalation/deintercalation reactions enable introduction/removal of intercalants without destructive structure transformation of host lattices. They are among the most versatile ways to design metastable phases attainable in mild synthesis conditions. Recently, topochemical deintercalation of oxygen anions has opened up an avenue to access new compounds with unusual transition metal oxidation states and interesting properties. So far, the scope of such anion deintercalation was mainly restricted to oxides and their oxyhalide derivatives. But lately we presented a proof of concept study on sulfur deintercalation reaction driven by anionic redox in $La_2O_2S_2$. Here we extend this work and present the design of new members of a family of slightly colored non-centrosymmetric metastable oxysulfides. Our work shows that the reduction with an alkali metal of sulfur dimers in $Ln_2O_2S_2$ (Ln = Pr, Nd) precursors leads to the topochemical deinsertion of half sulfur atoms of each S2 pairs, producing two new metastable *oA*-Ln_2O_2S (Ln= Pr, Nd) phases. The non-centrosymmetric compounds *oA*-Ln_2O_2S (Ln= La, Pr, Nd) evidence second and third harmonic generation effect, suggesting potential applicability of the topochemical route for design of nonlinear optical materials.

INTRODUCTION

Intercalation and deintercalation of a cationic guest (intercalant) are soft chemical processes often at work in lamellar materials without destroying the overall crystal structure of host lattices. That type of reactions draws even more public attention for its use in electrochemical devices after 2019 Nobel Prize. [1] Meanwhile, (de)intercalation processes have been serving as a powerful tool on conception of new solid-state materials. Intercalation / deintercalation reactions usually proceed at much lower temperature than conventional ceramic syntheses and are considered as typical soft chemistry (“Chimie douce”) method. Since in most cases the structural transformations are not destructive these reactions often lead to metastable compounds. For instance low temperature deintercalation of A^+ cations from transition metal dichalcogenides AMS_2, led to numerous metastable MS_2 edifices. Metastable CdI_2-type VS_2 and $CrSe_2$ were indeed obtained by deintercalation of $LiVS_2$ and $KCrSe_2$ in presence of iodine [2, 3] while cubic TiS_2 was prepared from $CuTi_2S_4$ using bromine as oxidizing agent.[4,5]

More recently, the deintercalation of oxygen anions via the use of metal hydrides have also attracted much attention due to the capability of the process to prepare metastable compounds with unusual transition metal oxidation states and interesting properties.[6, 7] Hence, the low temperature (T = 200 °C) oxygen deintercalation in the perovskite nickelate using NaH as reducing reagent,[7] led recently to the stunning discovery of the superconducting $Nd_{0.8}Sr_{0.2}NiO_2$ compounds with nickel in square planar coordination [8].

Most of topochemical intercalation reactions, as those aforementioned, rely on redox activity of transition metal cations. This is due both to the well-known, intrinsic ability of transition metals to accept different valence states. In contrast, monoatomic anions with fully occupied valence levels cannot play the role of redox center due to a too high redox potential in their fully reduced form (e.g. O^{2-}, S^{2-}). However, anions also exist in some materials such as chalcogenides and pnictides as molecular dimeric species, [9, 10] that is, as discrete and covalently-bonded structural entities that have vacant antibonding molecular orbitals available for electron transfer. The redox activity of such polyanionic species was first established in the 80’s, when Brec et al. succeeded in the fully deintercalating of lithium in the Li_2FeS_2 ternary sulfide. [11,12] This work demonstrated the valence change of the sulfur anions thanks to the formation of sulfur dimers $(S_2)^{2-}$ within the delithiated compound. Since then, the redox activity of anionic dimers or oligomers was observed in many polychalcogenides,[10] and was found more recently to play an important role in Li-rich oxides. [13,14] The intense researches on the redox activity of anions in both oxides [13, 15] and chalcogenides [16,17] has established itself as a very active new domain called “anionic redox”. In that framework some work is now focusing on the topochemical intercalation of metal species based on anionic redox only. In particular, it was shown that chalcogen dimers $(Q_2)^{2-}$ (Q = S, Se) embedded in lamellar compounds are effective anionic redox centers towards reductant metal species (M^0). [18] For example, the low temperature reaction of metallic copper (Cu^0) with $La_2O_2S_2$, a layered materials with $^2/_\infty[La_2O_2]$ slab well separated by $(S_2)^{2-}$ dimers, leads to the topochemical insertion of copper to form

$La_2O_2Cu_2S_2$. This process is driven by electron donation from elemental copper to the empty molecular orbital of $(S_2)^{2-}$ dimers, which triggers both the cleavage of S-S bonds and the migration of metal to construct infinite copper sulfide layers (Figure 1).

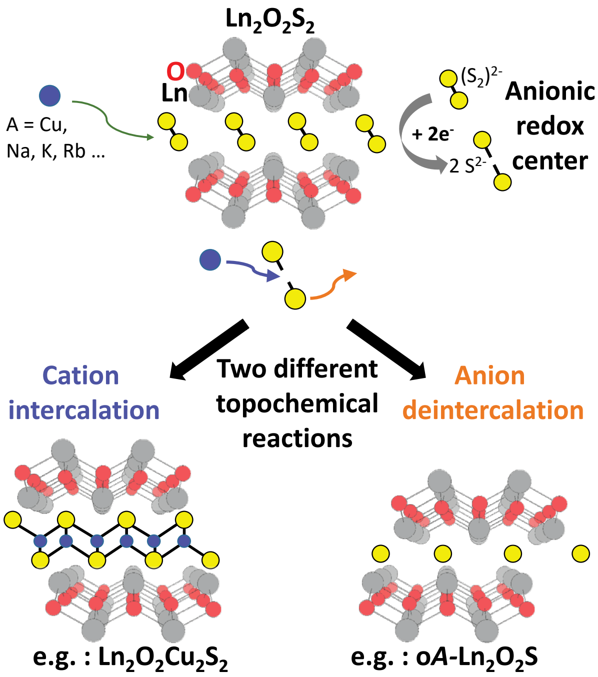

Figure 1. Illustration of the two different anionic redox topo chemical routes enabled by the reaction of chalcogenide dimer with different metal species. Breaking of the chalcogen-chalcogen bonds is followed either by intercalation of the metal species or by deintercalation of the part of its anions.

On the other hand, the reactivity of these $(S_2)^{2-}$ dimers can also lead to deintercalation of sulfur anions instead of intercalation of the metal species (Figure 1).[19] In this work, we follow our preliminary investigation of the deintercalation of sulfur in *La*$_2$O$_2$S$_2$, [19] to show that the whole series of isostructural homologues *Ln*$_2$O$_2$S$_2$ (*Ln*= La, Pr, Nd) equally undergo deintercalation of sulfur anions when treated with alkali metals (Na, K, Rb) at mild temperature. This topochemical reaction is reversible and conserves the structural features of the Ln_2O_2 layers (*vide infra*). At the end, the anionic redox reaction produces a family of metastable compounds hereafter labeled *oA*-Ln_2O_2S (notation by Pearson symbol) that are non-centrosymmetric compounds and potentially interesting as nonlinear optical materials.

Experimental section

Preparation of the $La_2O_2S_2$ precursors.

The synthesis of pure $Ln_2O_2S_2$ precursors (Ln=La, Pr, Nd) was performed in vacuum sealed tubes containing a mixture of Ln_2O_3, Ln and S (Ln_2O_3 from Aldrich 99.9%, Ln from Alpha Aesar 99.9% and S from Aldrich 99.99%) in stoichiometric ratio and annealed at 650°C during 120 hours.

Topochemical conversion from $Ln_2O_2S_2$ to oA-Ln_2O_2S.

The topochemical synthesis of oA-Ln_2O_2S (Ln=La, Pr, Nd) metastable compounds was carried out by mixing the $Ln_2O_2S_2$ precursors with one alkali metal (Li (Aldrich, 99%), Na (Aldrich, 99%), K (Aldrich, 98%) or Rb (Aldrich, 98%)) in a 1: 2 molar ratio. The mixtures prepared under argon atmosphere were then loaded into silica tubes that were evacuated (~10^{-3} torr) and sealed. The sealed tubes were then heated at temperature ranging from 200 °C to 350°C and held at that temperature for 2 h to 10 h (*e.g.* 340°C during 10h for most samples). Finally, the sealed tubes were gradually cooled to room temperature and subsequently opened under argon atmosphere. The resulting powders were successively washed with isopropanol, ethanol and distilled water to dissolve the alkali salts formed during the reaction and then dried in an oven at 60°C. When using Na, K or Rb this method yielded pure *oA*-Ln_2O_2S (Ln=La, Pr, Nd) compounds. The same method was tested for a mixture of Lithium and $La_2O_2S_2$ but an incomplete reaction was observed. It led to partial sulfur deintercalation of the oxysulfide precursor and to a passivation layer on the remaining Li metal pieces. The *oA*-Ln_2O_2S (Ln=La, Pr, Nd) powders are transparent but their color depends on the rare earth used *i.e.* colorless for Ln=La, slightly greenish Ln= Pr or slightly bluish for Ln= Nd. All products are stable under ambient atmosphere. In the case of $Ln_2O_2S_2$ the same reaction performed at 200°C or 350 °C gave identical results, i.e. pure *oA*-La_2O_2S without any trace of *hP*-La_2O_2S.

Intercalation of sulfur anions into oA-Ln_2O_2S (Ln=La, Pr).

The *oA*-Ln_2O_2S (*ca.* 200 mg) powders (Ln=La, Pr) were combined with S flakes (Aldrich, 99.99+%) in a 1 : 0.5 or 1 : 1 molar ratio and ground in an agate mortar under argon atmosphere. Then the mixture was pressed into pellets and sealed in an evacuated (~10^{-3} torr) silica tube. The tubes were heated to 200 °C at a rate of 100 °C h^{-1} and held at this temperature between 2 h and 4 h before gradual cooled down to room temperature. This method yielded pure powders of $Ln_2O_2S_2$ (Ln=La, Pr) when a *oA*-Ln_2O_2S : S ratio 1 : 1 was used for complete intercalation (see figure S5). Conversely when a half intercalation was targeted using a *oA*-Ln_2O_2S : S ratio 1 : 0.5 a new phase with formulation *oA*-$Ln_4O_4S_3$ was obtained often with traces of the *oA*-Ln_2O_2S precursor (see figure S6). In the case of *oA*-Ln_2O_2S a sulfur intercalation was also successfully attempted at lower temperature T = 150 °C but it required longer annealing time (48 h).

Preparation of stable hP-La_2O_2S compounds.

Stable hP-Ln_2O_2S (Ln=La, Pr, Nd) were obtained by decomposition of the $Ln_2O_2S_2$ precursors at 900°C. $Ln_2O_2S_2$ precursors we pressed into pellets and loaded into silica tubes that were sealed under vacuum (~10^{-3} torr). The tubes were heated at 900°C using a ramp of 100°C/hours and then held at this temperature for 2 hours. After cooling to room temperature a sulfur deposition was observed at one tube end. The powders obtained at the other tube extremities were pure hP-Ln_2O_2S compounds as confirmed by XRD analysis (see Figure S7).

Alternatively, the stable hP-Ln_2O_2S (Ln=La, Pr, Nd) polymorphs were also obtained by transformation of oA-Ln_2O_2S metastable phases. For these experiments a pressed pellet of oA-Ln_2O_2S were loaded into vacuum-sealed silica tubes (~10^{-3} torr), and held for 2 hours at 400°C. After cooling at room temperature, a pure powder of hP-Ln_2O_2S compound was obtained as characterized by XRD (see Figure S8).

Chemical analysis

Semiquantitative chemical analyses of all oA-Ln_2O_2S (Ln=La, Pr, Nd) samples, were performed using a scanning electron microscope JEOL 5800 equipped with an energy dispersive X-ray (EDX) microanalyzer. The chemical analysis of oA-Ln_2O_2S revealed the presence of the three elements Ln, O and S but due to the low atomic number of oxygen a quantitative result was not obtained for this element. The relative atomic percentage ratios (Ln/S) measured for the different La, Pr, Nd derivatives are respectively La/S= 64.4 (2)/35.6(1), Pr/S= 65.2(2)/34.8(1) and Nd/S= 66.5(4)/33.5(2). Assuming two lanthanum and oxygen in the atomic composition the EDX analysis gave the following compositions $La_2O_2S_{1.09(1)}$, $Pr_2O_2S_{1.06(1)}$,$Nd_2O_2S_{1.01(2)}$ in good agreement with the expected one oA-Ln_2O_2S.

Raman spectroscopy

Raman spectra of all samples were recorded in backscattered geometry using a Renishaw inVia spectrometer equipped with a 514 nm argon laser. The laser power was maintained at 0.15 mW. At least two different locations of the different powder samples were analysed to ensure their homogeneity.

Magnetic measurements

Magnetic measurements were performed using a Quantum Design MPMS SQUID magnetometer in the 300K-1.5K temperature range. Zero field-cooled (ZFC) and field-cooled (FC) susceptibility were measured on a powder sample of *oA*-Pr_2O_2S (m = 55.6 mg) under an applied field of 1000 Gauss. Data were corrected from the sample holder contribution. The core diamagnetism was calculated using tabulated Pascal increments. and a contribution $\square_{dia}$ of -9.4 × 10^{-5} cm^3/mole was subtracted from the measured data.

Diffuse-reflectance spectroscopy

The diffuse-reflectance spectra of all samples were recorded on a Varian Cary 5G spectrometer equipped with a 60 mm diameter integrating sphere and computer controlled using the Cary WinUV software. Diffuse reflectivity was collected from 250 nm to 1000 nm (i.e. 1.24 eV – 4.96 eV). The sample reflectance *R* was calibrated using Halon powder (Varian) as the reference of 100% reflectivity and plotted as the Kubelka-Munk function $K / S = (1 - R)^2 / (2R)$. Estimation of optical band gap E_g was directly made from Kubelka-Munk function K / S without converting them into Tauc plots.

SHG measurements

The SHG measurements were performed at room temperature using an optical parametric amplifier (Spectra Physics TOPAS Prime) excited by a titanium sapphire regenerative (Ti-Sap) amplifier (Spectra Physics Solstice) as the excitation light source, with 100 fs pulse width, 1 kHz repetition rate, 1.0 mJ=(pulse·cm2) excitation density, and wavelengths of 1200 nm. Sample luminescence was monitored using a spectrometer (Jovan-Ybon Triax550) equipped with a charge-coupled device (Andor Technology DU420A).

RESULTS AND DISCUSSION

$Ln_2O_2S_2$ (Ln=La, Pr, Nd) is a series of compounds to test anionic redox reactivity. These compounds are all isostructural with $La_2O_2S_2$ ($La^{3+}{}_2O^{2-}{}_2(S_2)^{2-}$) and possess a layered structure with sulfur-sulfur dimers sandwiched by Ln_2O_2 fluorite type layers. [20] The electronic band structure of these compounds reveal that the empty $\sigma_{S\text{-}S}$* and filled $\pi_{S\text{-}S}$* bands are laying on both sides of the Fermi level. [21] It means that the only redox active species in this material is the anionic sulfur dimer $(S_2)^{2-}$ that has its highest σ^* level available to host electrons of a reductant.

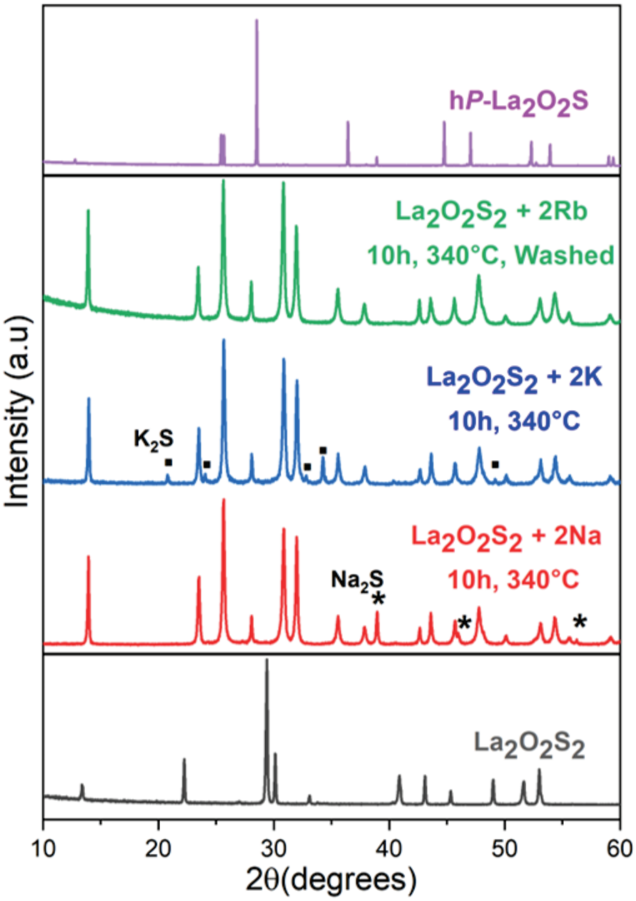

Figure 2. X-Ray diffraction patterns obtained after reaction of $La_2O_2S_2$ with alkali metals A= Na, K (before washing), Rb (after washing) at 340°C during 10h. The lower panel shows for comparison the X-Ray pattern of the precursor $La_2O_2S_2$ while the upper panel shows the pattern of the known compound hP-La2O2S.

In this study we have first tested the reactivity of the $La_2O_2S_2$ precursor toward the electropositive alkali metals i.e. A = Na, K, Rb. Our preliminary results conducted at low temperature (200 °C) with rubidium demonstrated the sulfur deintercalation from the precursor. [19] The same can be observed when Na or K alkali metals were used as reducing agents. Their synthesis conditions are detailed in the experimental part in SI.

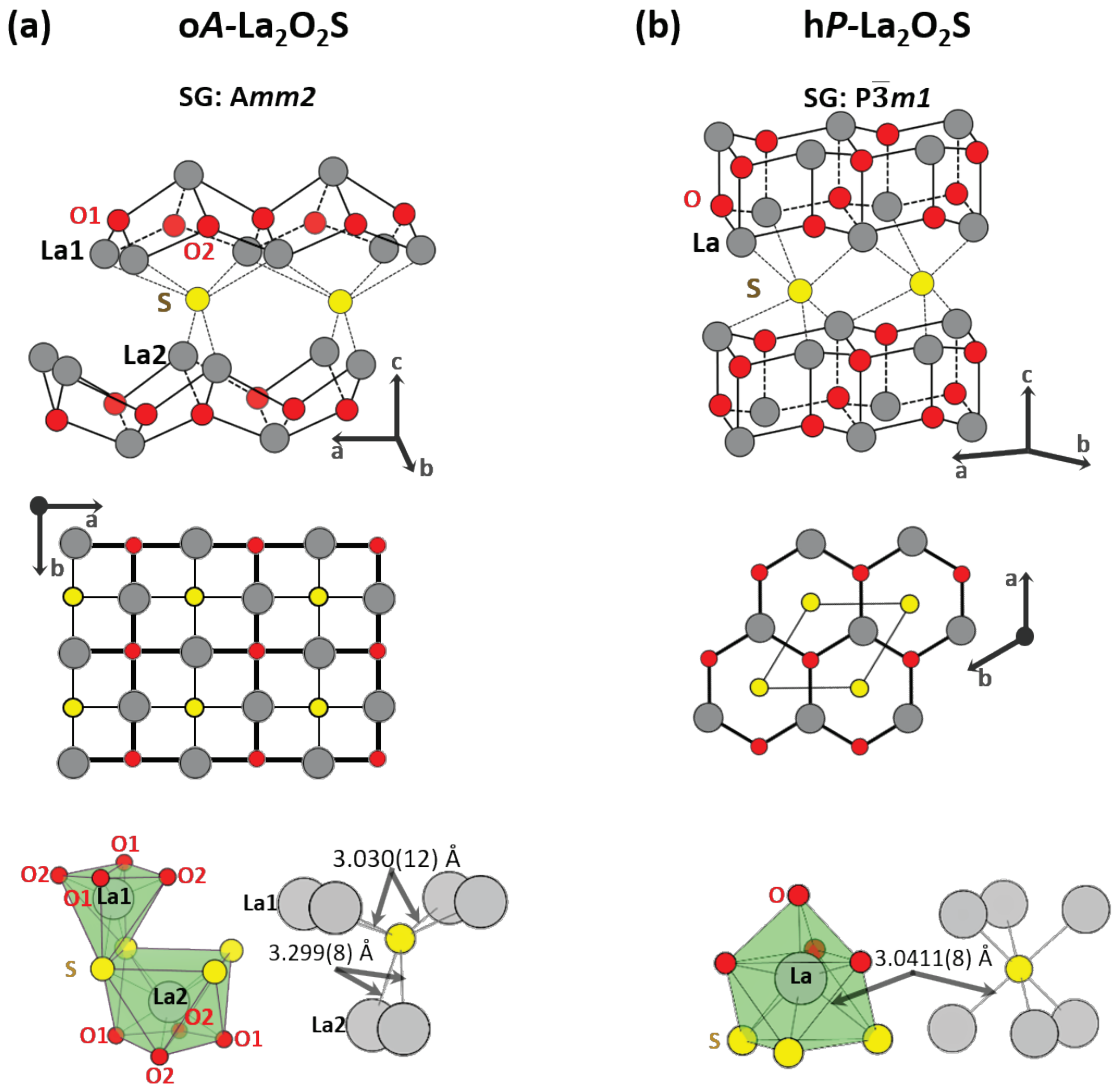

Figure 3: (a) Representation of the structure of the oA-La$_2$O$_2$S phase. The structure is projected along the b and c directions and the coordination polyhedra of the La and S atoms are shown. (b) Comparison with the structure of the stable phase hP-La$_2$O$_2$S.

Figure 2 compares the X-ray diffraction patterns of the products obtained when reacting with Na, K and Rb. These syntheses yielded the same product with appearance of A$_2$S alkaline salts that drive the reaction (see the Na and K reactions). These salts could be washed away with isopropanol (see the reaction with Rb for instance).

The results obtained with (A = Na, K, Rb) points towards the formation of La$_2$O$_2$S, which was fully confirmed by energy disperse X-ray spectroscopy (EDX) experiments (see supplementary information). The formation of these products is remarkable as their X-ray diffraction patterns are not comparable with the one of thermodynamically stable polymorph *hP*-La$_2$O$_2$S (see comparison in Figure 2) whose structure depicted in Figure 2 crystallizes in the hexagonal space group P-3m1. The reactivity of Pr$_2$O$_2$S$_2$ and Nd$_2$O$_2$S$_2$ towards alkali metals was equally examined (See SI for the detailed synthetic protocols). In both cases, the results are similar to the one observed with the La$_2$O$_2$S$_2$ precursor. The X-Ray diffraction patterns of all *Ln*$_2$O$_2$S compounds look quite similar (See Figure S1) with that of the lanthanum counterpart while the EDX confirm the formation of Pr$_2$O$_2$S and Nd$_2$O$_2$S (see analysis results in SI). In fact, these patterns correspond to the one of the new polymorph of La$_2$O$_2$S that was successfully predicted using the genetic algorithm USPEX (see reference 19 for details). This calculation revealed a metastable phase lying just above in energy of the stable phase hP-La$_2$O$_2$S. Figure 3 shows the structure of this predicted metastable phase called hereafter *oA*-La$_2$O$_2$S as it possess an orthorhombic space group *Amm*2. The predicted structure of oA-La$_2$O$_2$S was used as first model to refine the X-ray powder diffraction patterns of all *Ln*$_2$O$_2$S (Ln=La, Pr, Nd) compounds. These refinements converged rapidly and gave satisfying results as shown in Table 1 and Figure 4. The results of the refinements are summarized in Table 2 and Table 3. More details are given in supplementary information (Table S1, S2 and S3).

The reactivity of the pairs was also monitored using Raman spectroscopy. Figure S2 compares the Raman signature of all precursors Ln$_2$O$_2$S$_2$ (Ln=La, Pr, Nd) with the one of the metastable Ln$_2$O$_2$S phases. In the precursors, the stretching modes of the S-S bonds appears as the most prominent doublet peak around 500 cm^{-1}. This doublet completely disappears in all metastable Ln_2O_2S (Ln=La, Pr, Nd) phases. The Raman study confirms therefore that the reaction of alkali metals with the $Ln_2O_2S_2$ precursors ends up in the breaking of all the S-S dimers. It suggests that the reaction involves only the valence change of the anions from $(S_2)^{2-}$ to S^{2-}. This hypothesis is supported by magnetic susceptibility measurements specifically carried out on the Pr_2O_2S compound. Figure S3 shows that the magnetic susceptibility of this compounds follows a Curie-Weiss law, $\chi = C/(T - \theta)$ in the whole temperature range (4-300K). The Weiss temperature θ= 24.79 K is positive indicating the presence of ferromagnetic interaction. The experimental effective magnetic moments μ_{eff} = 3.47 μB deduced from the curie constant C= 1.5 cm^3 K mol^{-1} C is in good agreement with the effective magnetic moments calculated for Pr^{3+} ions (μ_{eff}^{calc} = 3.58 μB). It excludes therefore a valence change of the praseodymium cation during the sulfur deintercalation reaction.

Table 1. Cell parameters and reliability factor of o*A*-La_2O_2S, o*A*-Pr_2O_2S and o*A*-Nd_2O_2S obtained from the Rietveld refinement.

	o*A*-La2O2S	o*A*-Pr2O2S	o*A*-Nd2O2S
a	4.1489(3) Å	4.0899(4) Å	4.0647(5) Å
b	3.9752(3) Å	3.9043(4) Å	3.8738(4) Å
c	12.7275(9) Å	12.4665(11) Å	12.4050(15) Å
χ2	1.38	2.07	2.11
R(obs)(%)	1.87	1.95	3.57
R_p(%)	6.68	5.69	6.40
R_{wp}(%)	9.07	7.54	8.61

Table 2. Atomic positions and atomic displacement parameters of o*A*-La_2O_2S, o*A*-Pr_2O_2S and o*A*-Nd_2O_2S obtained from the Rietveld refinement. The occupied Wyckoff Position of the Amm2 space group are 2a (0 0 z) and 2b (½ 0 z). All site occupations were fixed to 1.

		o*A*-La_2O_2S		o*A*-Pr_2O_2S		o*A*-Nd_2O_2S	
Atoms	Site	z	Uiso(Å²)	z	Uiso(Å²)	z	Uiso(Å²)
Ln1	2a	0.6442(2)	0.0149(8)	0.6442(2)	0.0150(10)	0.6447(4)	0.0126(10)
Ln2	2b	0.3380(2)	0.0149(8)	0.3370(2)	0.0150(10)	0.3375(3)	0.0126(10)
O1	2a	0.236(3)	0.007(8)	0.229(4)	0.006(13)	0.233(6)	0.009(17)
O2	2b	0.218(3)	0.007(8)	0.212(4)	0.006(13)	0.213(6)	0.009(17)
S	2a	0.9665(10)	0.0066(1)	0.9674(14)	0.022(7)	0.969(2)	0.024(11)

Table 3. Main interatomic distances (Ln-O), (Ln-S), (Ln-Ln) and (S-S) for o*A*-La_2O_2S, o*A*-Pr_2O_2S and o*A*-Nd_2O_2S.

		Interatomic distance (Å)		
Atom 1	Atom 2	o*A*-La_2O_2S	o*A*-Pr_2O_2S	o*A*-Nd_2O_2S
Ln1	O1	2.31(3)	2.22(2)	2.23(4)
Ln1	O2	2.29(2)	2.21(2)	2.20(3)
Ln1	S	3.030(12)	2.945(14)	2.92(2)
Ln2	O1	2.44(3)	2.45(3)	2.41(4)
Ln2	O2	2.48(3)	2.50(3)	2.48(5)
Ln2	S	3.299(8)	3.261(9)	3.244(14)
Ln1	Ln2	3.780(2)	3.711(3)	3.688(4)
S	S	3.9752(5)	3.9043(7)	3.8738(9)

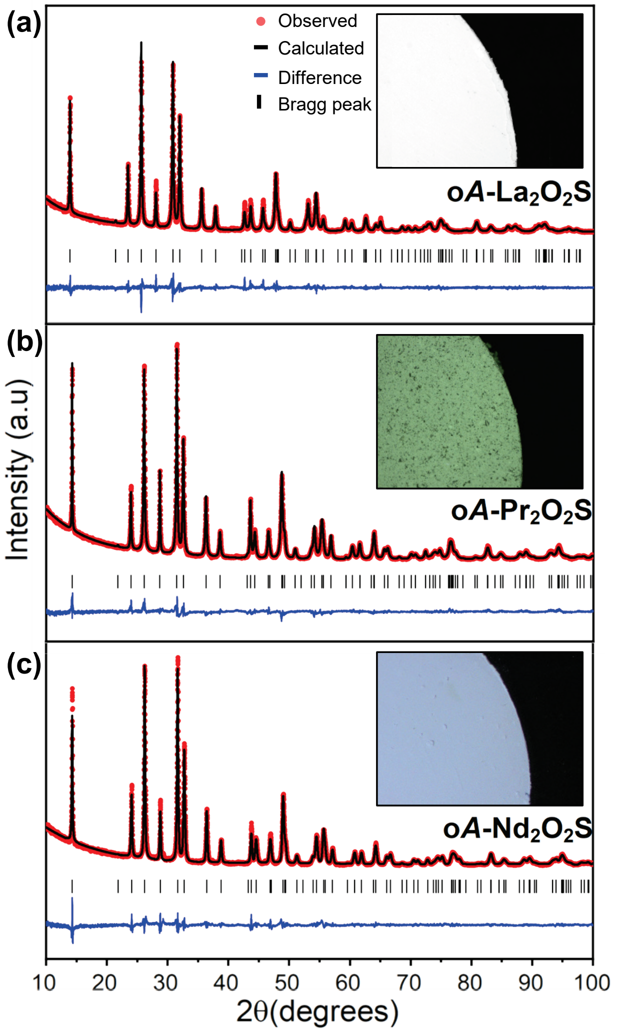

Figure 4. Rietveld refinement of the X-ray powder pattern of the oA-Ln_2O_2S (Ln=La, Pr, Nd) phases. (a) La compound, (b) Pr compound and (c) Nd compound. For each compound the insert shows a picture of a pressed pellet of the powder.

All these measurements suggest therefore a reaction based on a pure anionic redox mechanism that may be written:

$$Ln_2O_2(S_2)^{2-} + A \rightarrow Ln_2O_2S^{2-} + A_2S^{2-}$$

with Ln=La, Pr, Nd and A= Na, K, Rb.

This reaction leads to the deintercalation of half of the sulfur atoms from $Ln_2O_2S_2$ and produce a new polytype of *Ln*$_2$O$_2$S, i.e. *oA*-Ln_2O_2S (see Figure 2). All *oA-Ln*$_2$O$_2$S (*Ln*=La, Pr, Nd) compounds crystallize in the non-centrosymmetric space group *Amm*2 and are isostructural. As expected for steric reasons, Table 1 reveals that the cell parameters and cell volumes decrease going form the La to the Pr and Nd variants. The structural arrangement of the new oA-Ln_2O_2S compounds (Figure 3) is built upon the stacking of [Ln_2O_2] slabs alternating with isolated sulfur atoms. Both hP- and oA-Ln_2O_2S polymorphs are common in such alternate stacking while structures within the respective [Ln_2O_2] slabs differ drastically. Namely, the oA-Ln_2O_2S compound exhibits [Ln_2O_2] fluorite-type (001) slabs, while the hP derivatives exhibits [Ln_2O_2] fluorite-type (111) slabs. Consequently, the sulfur atoms present different lanthanide polyhedra in the two polymorphs, i.e. trigonal prism in the oA phase and octahedron in the hP phase (see Figure 3). The Ln atoms show also different environments. In the hP structure type, Ln atoms occupy a single coordination site composed of four oxygen atoms and three sulfur atoms. In contrast, there are two different Ln sites in the oA-structure type composed of four oxygen atoms and two or three sulfur atoms (see Figure 3). Clearly the oA-La_2O_2S phase is directly inherited from the $La_2O_2S_2$ precursor built up from an alternate stacking of (001) fluorite-type [La_2O_2]$^{2+}$ infinite layers separated from each other by discrete $(S_2)^{2-}$ sulfur dimers aligned in parallel to the layers. [20] The sulfur deintercalation does not modify therefore the [La_2O_2] slab but only involves a shift of half [La_2O_2] layers along the ½(b + c) direction of the precursor as shown in Figure S4.

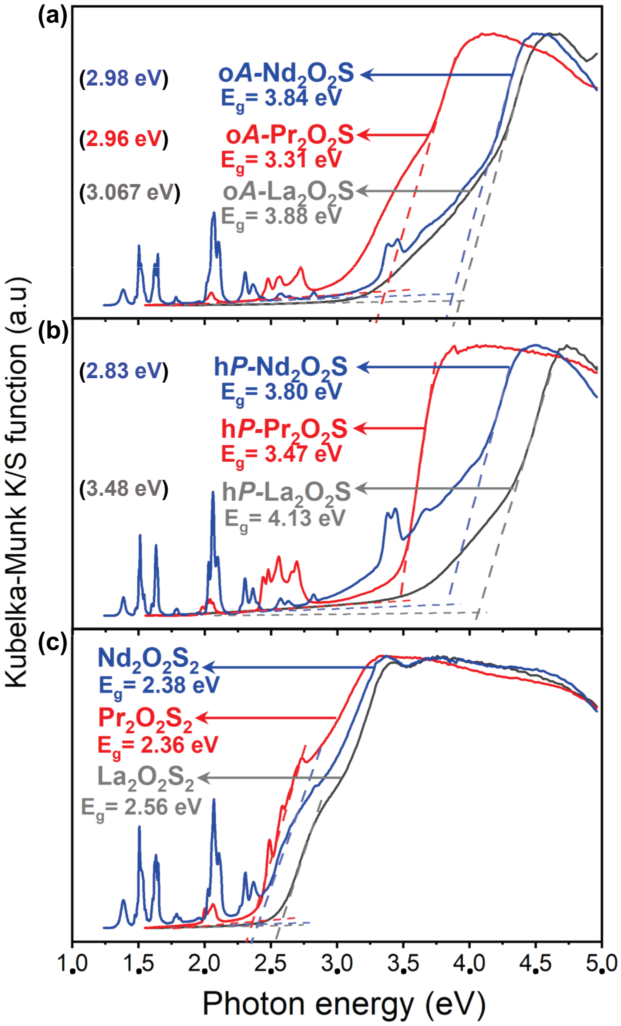

Figure 5 : Diffuse-reflectance spectra measured on (a) oA-Ln_2O_2S (b) hP-Ln_2O_2S and (c) $Ln_2O_2S_2$ (Ln = La, Pr, Nd)~~.~~ The band gap energies (Eg) of all compounds are indicated in each panel and their pre-peak energies are put in parentheses when necessary.

This observation supports the topochemical nature of the sulfur deintercalation reaction. To learn more about this process, we investigated the low temperature reversibility of the reaction i.e. the sulfur intercalation into oA-Ln_2O_2S.

To this end, the powders oA-Ln_2O_2S easiest to synthesize (*i.e.* with Ln= La, Pr) were mixed with elemental sulfur in the 1:1 atomic ratio and heated at 200 °C. The XRD analysis of the products (Figure S5) confirmed the back conversion to the original $Ln_2O_2S_2$ materials with no detected impurities. These experiments confirm the complete reversibility of the temperature-assisted sulfur intercalation/deintercalation reaction based on a pure anionic redox process. Moreover partial intercalation or deintercalation experiments undertaken with oA-La_2O_2S have shown that the reaction involves the formation of at least one intermediate phase with composition $La_2O_2S_{1.5}$ (i.e. $La_4O_4S_3$, $Ln^{3+}{}_4O^{2-}{}_4(S_2)^{2-}S^{2-}$) (see Figure S6). The structure of this intermediate phase $La_4O_4S_3$ is also inherited from the $Ln_2O_2S_2$ precursor (see ref 19 for structure determination). The same behavior is also observed in the case of partial intercalation experiments undertaken with oA-Pr_2O_2S. The diffraction pattern evidences new peaks in good agreement with the simulated pattern of a $Pr_4O_4S_3$ phase (SG=*Amm2*; a=8.3546(13), b=3.9773(5), c= 12.5481(13)) isostructural with $La_4O_4S_3$ (see Figure S6).

Figure 4 displays in inserts the pictures of pressed pellets of oA-Ln_2O_2S powders. The La derivative is colorless while the Pr and Nd derivatives show, respectively a slight green and blue hue coming from the 4f transitions on the lanthanide ions. The Kulbelka-Munk transformed diffuse-reflectance spectra of oA- and hP-Ln_2O_2S powders, as well as their $Ln_2O_2S_2$ precursors are displayed in Figure 5. The synthesis conditions for preparation of the stable *hP*-Ln_2O_2S compounds is described in supplementary information and their powder X-ray diffraction patterns are displayed in Figures S7 and S8. All Ln_2O_2S samples except hP-Pr_2O_2S exhibit an absorption preceded by a pre-peak. Overall absorption shift towards high energies along the Pr < Nd ~ La sequences for the oA-series with pre-peaks and absorption thresholds at 2.96 and 3.31 eV, 2.98 and 3.84 eV and 3.07 and 3.88 eV for oA-Pr_2O_2S, Nd_2O_2S and La_2O_2S, respectively. In contrast, the absorptions associated to hP-Nd_2O_2S (2.83 and 3.80 eV) are significantly lower in energy than the ones hP-La2O2S (3.48 and 4.13 eV) while hP-Pr_2O_2S exhibit only a steep onset at 3.47 eV. Sharp and low-intense absorptions are observed in the visible range for Nd and Pr containing Ln2O2S phases in relation with Laporte forbidden f-f transitions. Their weakness account for the pale observed green and blue colors for Pr_2O_2S and Nd_2O_2S. These bands are located at the same energy for the oA- and hP- polymorphs and the $Ln_2O_2S_2$ precursors for Pr and Nd lanthanides. $La_2O_2S_2$, $Pr_2O_2S_2$ and $Nd_2O_2S_2$, display a yellow color associated to $\pi_{S\text{-}S}^* \rightarrow \sigma_{S\text{-}S}^*$ transitions.

Given their (almost) colorless and non-centrosymmetric character, the oA-Ln_2O_2S powders were subsequently tested for the possible generation of light with a doubled frequency (second harmonic generation, SHG). Figure 6 shows the non-linear optical responses of oA-Ln_2O_2S samples in the 350-700 nm range for excitation at 1200 nm at room temperature. These measurements evidence that all oA-Ln_2O_2S compounds exhibit a SHG activity at 600 nm, which is consistent with their non-centrosymmetric structure. At the same time, a relatively large third harmonic generation (THG) peak is also observed at 400 nm for all compounds. THG is expected regardless the crystal symmetry but it is often studied in non-centrosymmetric ferroelectric crystals in order to take an advantage of their strong nonlinear light-matter interactions. [22] Accordingly, their THG signals became much weaker than SHG. On the contrary, many typical centrosymmetric crystals such as α-BBO, calcite, and rutile equally exhibit THG despite of their SHG inertness. [23]In particular, some centrosymmetric crystals like Cu_2O are known to exhibit strong THG signal with very weak signal at double frequency. [24]

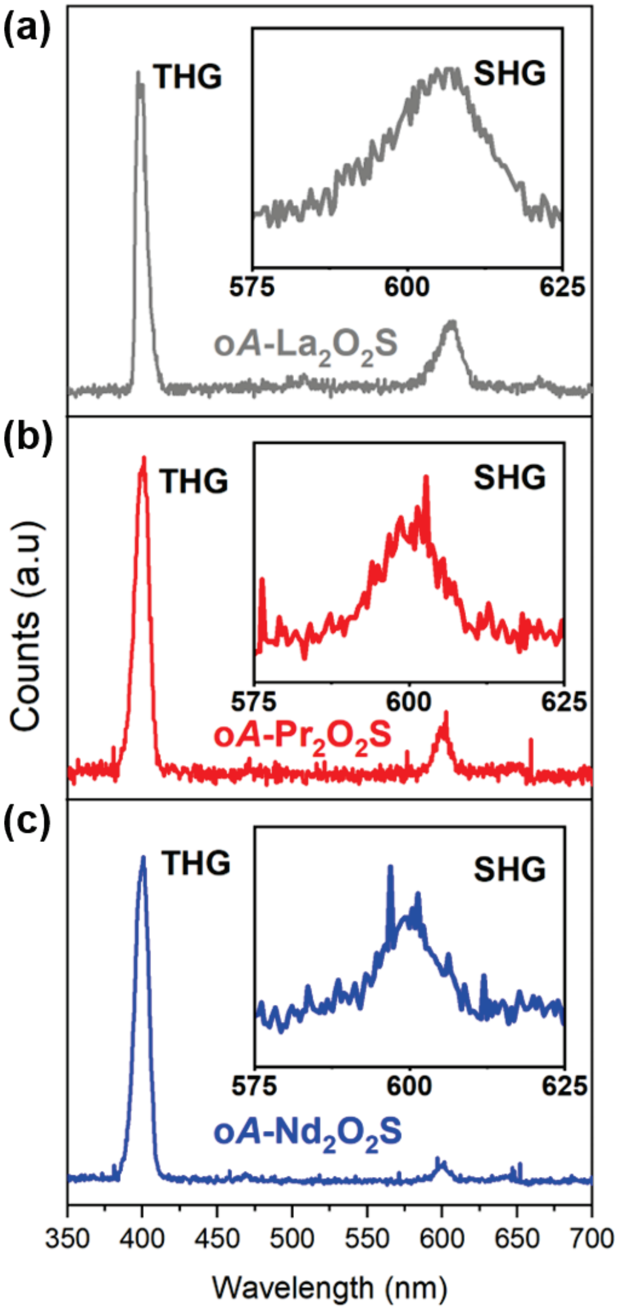

Figure 6 : Spectra of SHG and THG of oA-Ln2O2S compounds ((a) Ln=La; (b) Ln=Pr; and (c) Ln=Nd) under excitation at 1200 nm.

The spectra in Figure 6 resemble rather those centrosymmetric crystals despite the non-centrosymmetric crystal structure of oA-Ln_2O_2S. This contradictory feature implies that oA-Ln_2O_2S may exhibit exceptionally strong third-order optical susceptibility $\chi^{(3)}$, and/or a weak polar structure resulting in small $\chi^{(2)}$ coefficient. To gain insights into the weak SHG response, the dipole moments for LaO_4S_2 and LaO_4S_4 polyhedra were therefore calculated using a simple bond-valence approach.[25] The dipole moments of these polyhedra are estimated to be 1.71 and 2.16 D (Debye: 10^{-18} esu cm) in magnitude, respectively. This is smaller than typical dipole moments found in other mixed anion polar building blocks, e.g., 9.75-11.76 D for $GeOS_3$, [26] and 3.03-5.70 for $ZnOS_3$.[27] Furthermore, the dipole moments of the

La-centered polyhedra in oA-Ln_2O_2S are directed antiparallel to each other along the polar *c* axis, leading to weakening of the SHG response. Actually, the dipole moment induced by external electric field also plays a significant role in the SHG response, and thus these perturbation term should be considered to explain the observed magnitude of SHG and THG signals. [28]

Materials with large THG signals are of high interest to extend the frequency conversion processes and generate directly coherent laser light in the UV region from commercially available laser sources. [29,30] Indeed, there is nowadays a high demand for medical, chemical sensing or optical communication applications. In that context, the large THG signal observed in the oA-Ln2O2S compounds will require more investigation to fully characterize the NLO $\chi^{(3)}$ coefficients of these compounds. This behavior of the oA-Ln_2O_2S oxysulfide compounds recalls the recent discovery of a large THG signals in another oxysulfide $Ba_5(VO_2S_2)_2(S)_2$. [31] Moreover oxychalcogenides emerge as promising IR nonlinear optical (NLO) materials with good balance between large SHG coefficients and high laser damage threshold. [32,33,34] The search for new oxysulfides with NLO or other functional properties is therefore very promising. The sulfur deintercalation method described in this paper might be an interesting alternative to design such mixed anions functional materials. [35,36]

CONCLUSION

We have demonstrated that the topochemical deintercalation of sulfur from the $Ln_2O_2S_2$ compounds (Ln = La, Pr, Nd) can be triggered in presence of Rb, K and Na alkali metals. The reaction leads to a metastable form of the Ln_2O_2S compounds built on [Ln_2O_2] fluorite-type (001) slabs against [Ln_2O_2] fluorite-type (111) slabs in the stable form. The process is reversible, i.e. sulfur atoms can be deintercalated and reintercalated, and is based only on the anionic redox activity of sulfurs, i.e. the $(S_2)^{2-}/S^{2-}$ redox couple. The new topochemical Ln_2O_2S materials are non-centrosymmetric compounds. They evidence a SHG signature, but also a (very) strong THG signal. This opens the door of topochemical route to design nonlinear optical, oxysulfide materials for future applicability in optics.

ASSOCIATED CONTENT

Supporting Information.

Additional XRD patterns of the samples (Figure S1, S2 and S4 to S8). Susceptibility of oA- Pr_2O_2S compound (Figure S3). Hypothetical topochemical synthetic pathway of the sulfur deintercalation (Figure S4). Detailed Rietveld refinement results of the oA-Ln_2O_2S phases with *Ln*= La, Pr, Nd (Tables S1 to S3). This material is available free of charge via the Internet at http://pubs.acs.org.

AUTHOR INFORMATION

Corresponding Author

* Stephane.jobic@cnrs-imn.fr ; Laurent.cario@cnrs-imn.fr

Author Contributions

The manuscript was written through contributions of all authors. All authors have given approval to the final version of the manuscript.

ACKNOWLEDGMENT

The PhD grant of L-B M. was financially supported by the CNRS and the region Pays-de-la-Loire. This work was performed in the framework of the International Core-to-Core Project on Mixed Anion Research for Energy Conversion. Y.T. acknowledges the grant from the Murata Science Foundation.

TOC Graphic

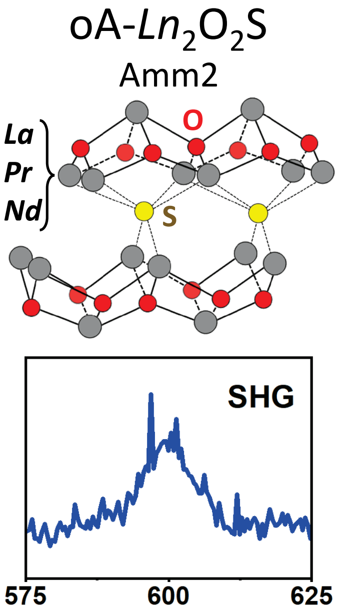

REFERENCES

1 Zhang, H.; Li, C.; Eshetu, G. G.; Laruelle, S.; Grugeon, S.; Zaghib, K.; Julien, C.; Mauger, A.; Guyomard, D.; Rojo, T.; Gisbert-Trejo, N.; Passerini, S.; Huang, X.; Zhou, Z.; Johansson, P.; Forsyth, M. From Solid-Solution Electrodes and the Rocking-Chair Concept to Today's Batteries. *Angew. Chem. Int. Ed.* **2020**, *59 (2)*, 534–538. https://doi.org/10.1002/anie.201913923.

2 Murphy, D. W.; Cros, C.; Di Salvo, F. J.; Waszczak, J. V. Preparation and Properties of Li_xVS_2 (0 .Ltoreq. x .Ltoreq. 1). *Inorg. Chem.* **1977**, *16* (12), 3027–3031.

3 van Bruggen, C. F.; Haange, R. J.; Wiegers, G. A.; de Boer, D. K. G. $CrSe_2$, a New Layered Dichalcogenide. *Physica B+C* **1980**, *99* (1), 166–172.

4 Schöllhorn, R.; Payer, A. C-TiS2, a New Modification of Titanium Disulfide with Cubic Structure. *Angew. Chem. Int. Ed.* **1985**, *24 (1)*, 67–68. https://doi.org/10.1002/anie.198500671.

5 Sinha, S.; Murphy, D. W. Lithium Intercalation in Cubic TiS_2. Solid State Ionics **1986**, *20 (1)*, 81–84. https://doi.org/10.1016/0167-2738(86)90038-X.

6 Tsujimoto, Y.; Tassel, C.; Hayashi, N.; Watanabe, T.; Kageyama, H.; Yoshimura, K.; Takano, M.; Ceretti, M.; Ritter, C.; Paulus, W. Infinite-Layer Iron Oxide with a Square-Planar Coordination. *Nature* **2007**, *450 (7172)*, 1062–1065. https://doi.org/10.1038/nature06382.

7 Hayward, M. A.; Green, M. A.; Rosseinsky, M. J.; Sloan, J. Sodium Hydride as a Powerful Reducing Agent for Topotactic Oxide Deintercalation: Synthesis and Characterization of the Nickel(I) Oxide $LaNiO_2$. *J. Am. Chem. Soc.* **1999**, 121 (38), 8843–8854. https://doi.org/10.1021/ja991573i.

8 Li, D.; Lee, K.; Wang, B. Y.; Osada, M.; Crossley, S.; Lee, H. R.; Cui, Y.; Hikita, Y.; Hwang, H. Y. Superconductivity in an Infinite-Layer Nickelate. *Nature* **2019**, *572 (7771)*, 624–627. https://doi.org/10.1038/s41586-019-1496-5.

9 Jobic, S.; Brec, R.; Rouxel, J. Occurrence and Characterization of Anionic Bondings in Transition Metal Dichalcogenides. Journal of Alloys and Compounds **1992**, *178 (1)*, 253–283. https://doi.org/10.1016/0925-8388(92)90269-F.

10 Rouxel, J. Anion–Cation Redox Competition and the Formation of New Compounds in Highly Covalent Systems. *Chemistry – A European Journal* **1996**, *2 (9)*, 1053–1059. https://doi.org/10.1002/chem.19960020904.

11 Dugast, A.; Brec, R.; Ouvrard, G.; Rouxel, J. Li2FeS2, a Cathodic Material for Lithium Secondary Battery. *Solid State Ionics* **1981**, *5*, 375–378. https://doi.org/10.1016/0167-2738(81)90271-X.

12 Brec, R.; Dugast, A.; Le Mehauté, A. Chemical and Electrochemical Study of the Li_xFeS_2 Cathodic System $(0 < x \leqslant 2)$. *Materials Research Bulletin* **1980**, *15 (5)*, 619–625. https://doi.org/10.1016/0025-5408(80)90142-7.

13 Assat, G.; Tarascon, J.-M. Fundamental Understanding and Practical Challenges of Anionic Redox Activity in Li-Ion Batteries. *Nature Energy* **2018**, *3 (5)*, 373. https://doi.org/10.1038/s41560-018-0097-0.

14 Sathiya, M.; Rousse, G.; Ramesha, K.; Laisa, C. P.; Vezin, H.; Sougrati, M. T.; Doublet, M.-L.; Foix, D.; Gonbeau, D.; Walker, W.; Prakash, A. S.; Ben Hassine, M.; Dupont, L.; Tarascon, J.-M. Reversible Anionic Redox Chemistry in High-Capacity Layered-Oxide Electrodes. *Nature Materials* **2013**, *12 (9)*, 827–835. https://doi.org/10.1038/nmat3699.

15 Ben Yahia, M.; Vergnet, J.; Saubanère, M.; Doublet, M.-L. Unified Picture of Anionic Redox in Li/Na-Ion Batteries. *Nature Materials* **2019**, *18 (5)*, 496–502. https://doi.org/10.1038/s41563-019-0318-3.

16 Shadike, Z.; Zhou, Y.-N.; Chen, L.-L.; Wu, Q.; Yue, J.-L.; Zhang, N.; Yang, X.-Q.; Gu, L.; Liu, X.-S.; Shi, S.-Q.; Fu, Z.-W. Antisite Occupation Induced Single Anionic Redox Chemistry and Structural Stabilization of Layered Sodium Chromium Sulfide. *Nat. Commun*. **2017**, *8 (1)*, 566. https://doi.org/10.1038/s41467-017-00677-3.

17 Leube, B. T.; Robert, C.; Foix, D.; Porcheron, B.; Dedryvère, R.; Rousse, G.; Salager, E.; Cabelguen, P.-E.; Abakumov, A. M.; Vezin, H.; Doublet, M.-L.; Tarascon, J.-M. Activation of Anionic Redox in D0 Transition Metal Chalcogenides by Anion Doping. *Nat. Commun.* **2021**, *12 (1)*, 5485. https://doi.org/10.1038/s41467-021-25760-8.

18 Sasaki, S.; Driss, D.; Grange, E.; Mevellec, J.-Y.; Caldes, M. T.; Guillot-Deudon, C.; Cadars, S.; Corraze, B.; Janod, E.; Jobic, S.; Cario, L. A Topochemical Approach to Synthesize Layered Materials Based on the Redox Reactivity of Anionic Chalcogen Dimers. *Angew. Chem. Int. Ed.* **2018**, *57 (41)*, 13618–13623. https://doi.org/10.1002/anie.201807927.

[19] Sasaki, S.; Caldes, M. T.; Guillot-Deudon, C.; Braems, I.; Steciuk, G.; Palatinus, L.; Gautron, E.; Frapper, G.; Janod, E.; Corraze, B.; Jobic, S.; Cario, L. Design of Metastable Oxychalcogenide Phases by Topochemical (de)Intercalation of Sulfur in $La_2O_2S_2$. *Nat Commun* **2021**, *12* (1), 3605. https://doi.org/10.1038/s41467-021-23677-w.

20 Ostoréro, J. & Leblanc, M. Room-temperature structure of LaO_2S_2. *Acta Cryst.* **1990**, *C46*, 1376–1378.

21 Mvélé, L.-B.; Sasaki, S.; Latouche, C.; Deniard, P.; Janod, E.; Braems, I.; Jobic, S.; Cario, L. Revisiting the Crystal Structure of Layered Oxychalcogenides $Ln_2O_2S_2$ (Ln = La, Pr, and Nd). *Inorg. Chem.* **2023**, *62* (19), 7264–7272. https://doi.org/10.1021/acs.inorgchem.3c00147.

22 (a) Y. Takagi et al. Journal of Luminescence 87, 865-867 (2000). (b) S.-N. Zhu et al. Science 278, 843-846 (1997). (c) B. Kukyk et al. *Mat. Chem. Phys.* **2010**, *120*, 114-117.

23 Li, K.; Lin, J.; Zhang, Z.; Sato, R.; Shimizu, H.; Matsukuma, H.; Gao, W. Investigation of Angle Measurement Based on Direct Third Harmonic Generation in Centrosymmetric Crystals. *Appl. Sci.* **2023**, *13*, 996. https://doi.org/10.3390/app13020996

24 Mani S. E.; Jang J. I.; Ketterson J. B. Large third-order susceptibility and third-harmonic generation in centrosymmetric Cu(2)O crystal. *Opt Lett.* **2009**, *34*, 2817-2819

25 Maggard, P. A.; Nault, T. S.; Stern, C. L.; Poeppelmeier, K. R. Alignment of Acentric $MoO_3F_3^{3-}$ Anions in a Polar Material: $(Ag_3MoO_3F_3)(Ag_3MoO_4)Cl$. *Journal of Solid State Chemistry* **2003**, *175* (1), 27–33. https://doi.org/10.1016/S0022-4596(03)00090-2.

26 Cui, S.; Wu, H.; Hu, Z.; Wang, J.; Wu, Y.; Yu, H. The Antiperovskite-Type Oxychalcogenides $Ae_3Q[GeOQ_3]$ (Ae = Ba, Sr; Q = S, Se) with Large Second Harmonic Generation Responses and Wide Band Gaps. *Advanced Science* **2023**, *10* (4), 2204755. https://doi.org/10.1002/advs.202204755.

27 Tsujimoto, Y.; Juillerat, C. A.; Zhang, W.; Fujii, K.; Yashima, M.; Halasyamani, P. Shiv.; zur Loye, H.-C. Function of Tetrahedral ZnS3O Building Blocks in the Formation of $SrZn_2S_2O$: A Phase Matchable Polar Oxysulfide with a Large Second Harmonic Generation Response. *Chem. Mater.* **2018**, *30* (18), 6486–6493. https://doi.org/10.1021/acs.chemmater.8b02967.

28 Jiang, X.; Zhao, S.; Lin, Z.; Luo, J.; Bristowe, P. D.; Guan, X.; Chen, C. The Role of Dipole Moment in Determining the Nonlinear Optical Behavior of Materials: Ab Initio Studies on Quaternary Molybdenum Tellurite Crystals. *J. Mater. Chem. C* **2013**, *2* (3), 530–537. https://doi.org/10.1039/C3TC31872A.

29 Jo, H.; Kim, H. G.; Byun, H. R.; Jang, J. I.; Ok, K. M. Synthesis, Structure, and Third-Harmonic Generation Measurements of a Mixed Alkali Metal Iodate, $KLi_2(IO_3)_3$. *Journal of Solid State Chemistry* **2020**, *282*, 121120.

[30] Mateos, L.; Ramírez, M. O.; Carrasco, I.; Molina, P.; Galisteo-López, J. F.; Víllora, E. G.; de las Heras, C.; Shimamura, K.; Lopez, C.; Bausá, L. E. $BaMgF_4$: An Ultra-Transparent Two-Dimensional Nonlinear Photonic Crystal with Strong $\chi^{(3)}$ Response in the UV Spectral Region. *Adv. Funct. Mater.* **2014**, *24 (11)*, 1509–1518. https://doi.org/10.1002/adfm.201302588.

[31] Almoussawi, B.; Huvé, M.; Dupray, V.; Clevers, S.; Duffort, V.; Mentré, O.; Roussel, P.; Arevalo-Lopez, A. M.; Kabbour, H. Oxysulfide $Ba_5(VO_2S_2)_2(S_2)_2$ Combining Disulfide Channels and Mixed-Anion Tetrahedra and Its Third-Harmonic-Generation Properties. *Inorg. Chem.* **2020**, *59* (9), 5907–5917. https://doi.org/10.1021/acs.inorgchem.9b03674.

[32] Liu, B.-W.; Jiang, X.-M.; Wang, G.-E.; Zeng, H.-Y.; Zhang, M.-J.; Li, S.-F.; Guo, W.-H.; Guo, G.-C. Oxychalcogenide $BaGeOSe_2$:

Highly Distorted Mixed-Anion Building Units Leading to a Large Second-Harmonic Generation Response. *Chem. Mater.* **2015**, *27* (24), 8189–8192. https://doi.org/10.1021/acs.chemmater.5b03649.

[33] Cheng, Y.; Wu, H.; Yu, H.; Hu, Z.; Wang, J.; Wu, Y. Rational Design of a Promising Oxychalcogenide Infrared Nonlinear Optical Crystal. *Chemical Science* **2022**, *13* (18), 5305–5310. https://doi.org/10.1039/D2SC00099G.

[34] Wang, R.; Liang, F.; Wang, F.; Guo, Y.; Zhang, X.; Xiao, Y.; Bu, K.; Lin, Z.; Yao, J.; Zhai, T.; Huang, F. $Sr_6Cd_2Sb_6O_7S_{10}$: Strong SHG Response Activated by Highly Polarizable Sb/O/S Groups. *Angewandte Chemie International Edition* **2019**, *58* (24), 8078–8081. https://doi.org/10.1002/anie.201902806.

35 Orr, M.; Hebberd, G. R.; McCabe, E. E.; Macaluso, R. T. Structural Diversity of Rare-Earth Oxychalcogenides. *ACS Omega* **2022**, *7* (10), 8209–8218. https://doi.org/10.1021/acsomega.2c00186.

[36] Harada, J. K.; Charles, N.; Poeppelmeier, K. R.; Rondinelli, J. M. Heteroanionic Materials by Design: Progress Toward Targeted Properties. *Advanced Materials* **2019**, *31* (19), 1805295. https://doi.org/10.1002/adma.201805295.